Received: xxx **Accepted:** xxx **Published:** xxx.
DOI. xxxxxxx
Volume xxx, Issue xxx, p.p. 1-27: xxx
Research Article
Open Access
Control and Optimization in Applied Mathematics - COAM

A Localized RBF-Partition of Unity Collocation Method for Elliptic PDE-Constrained Optimal Control

Maha M. Mohammed Ali

Department of Information and Communication Technology, Polytechnic College of Engineering Specializations, Middle Technical University, Baghdad, Iraq

✉ **Correspondence:**
Maha Mohsin Mohammed Ali
E-mail:
maha.ali2015.ma@mtu.edu.iq

How to Cite
Mohsin Mohammed Ali, M. (2027). "A localized RBF-partition of unity collocation method for elliptic PDE-constrained optimal control". *Control and Optimization in Applied Mathematics*, XX(X), x–XX, 1–27. https://doi.org/10.30473/coam.2026.78551.1436

Abstract. The problem of numerically solving partial differential equations is precisely one of accuracy with an appropriate cost. While globally supported methods yield arbitrarily high-order accuracy, they are computationally infeasible with increasing grid-point, while locally supported schemes are efficient while potentially lacking high-order accuracy. The presented framework which proposes the localized meshless method that reduces such contradiction by combining a RBF approximation and the Partitions of Unity (PU) decomposition on several elliptic, convection-diffusion, and Helmholtz boundary value problems, as well as the associated PDE-constrained optimal control problems. Overlapping subdomains are chosen and each subdomain comprises of a locally fitted RBF expansion. It is then combined through the compactly supported PU weight functions. Localization-replacing one badly conditioned large dense global RBF collocated system by numerous well-conditioned small local ones, reducing the theoretical computational complexity from $\mathcal{O}(N^3)$ to $\mathcal{O}(N \log N)$. This framework is validated through three standard benchmark problems: Poisson's equation, a singularly perturbed convection-diffusion equation, and the Helmholtz equation on a circle, each within a distributed optimal control problem formulation. The proposed scheme achieves L^2-norm errors of order 10^{-4} at $N = 1{,}000$ nodes, outperforming both standard finite difference methods and global RBF collocation by factors of 28 to 49 in accuracy. Optimal control problems are handled through a Lagrange multiplier formulation yielding coupled state and adjoint systems, both discretized within the same RBF-PU architecture. The framework is illustrated through a detailed engineering case study — optimal heat-source regulation in a thermally loaded plate — in which the complete optimality system is derived, physically interpreted, and numerically solved. Numerical stability, current limitations, and directions for future investigation are discussed.

Keywords. Radial basis functions, Partition of unity, Meshless methods, PDE-constrained optimization, Optimal control, Convection-diffusion equations, Lagrange multiplier method.

MSC. 65N35; 49M25; 65N12.

1 Introduction

Partial differential equations (PDEs) are used extensively in a large number of scientific and engineering disciplines to model phenomena such as heat transfer, fluid motion, wave propagation, and optimization problems. Obtaining accurate numerical solutions remains non-trivial when the problem involves complex geometries or non-standard boundary conditions, such as moving boundaries. Established numerical discretization techniques such as the Finite Difference Method (FDM) or the Finite Element Method (FEM) have been applied successfully to a wide variety of problems. In these cases, however, a meshing procedure that creates a discrete computational mesh fitting the geometry of the domain must be established. For complex or moving-boundary domains, mesh generation and regeneration can become an expensive process that significantly compromises numerical accuracy. These difficulties have motivated the development of meshless methods as an appealing alternative. Meshless methods describe the domain using a set of scattered points and, in contrast to mesh-based methods, do not require nodal connectivity.

Of all, meshless methods for the numerical solution of partial differential equations by Radial Basis Function(RBF) which were successfully applied by researchers in decades has become increasingly popular. RBF methods for the numerical solution to differential equations are based upon the multiquadric interpolation scheme established by Hardy (1971), and first developed by means of the direct RBF collocation method based on a general framework of RBF to solve partial differential equations by Kansa [16]. An important desirable property of the RBF methods is the easiness in accommodating scattered data and even these approximations can be arbitrarily accurate for smooth problems. Basic disadvantage of a RBF method if implemented globally collocated manner is that the resulting matrix is numerically poorly conditioned as number of nodes is growing up, whose factorization is $\mathcal{O}(N^3)$. Selecting an appropriate shape parameter ε is one of the critical issues. When approximation is too excellent it leads to ill-conditioned matrices, whereas too poor one does not improve result and the accuracy will not be acceptable [9, 27].

These conditioning issues can be elegantly handled through a Partition of Unity (PU) based framework. The approach subdivides the computational domain into overlapping subdomains and generates a local RBF approximation on each subdomain. These local approximations are blended by smoothly and compactly supported weight functions that sum to one, thereby forming a partition of unity. This yields several small, well-conditioned systems instead of one large dense system. The PU framework was originally applied in the FEM context by Babuška and Melenk [1] and subsequently extended to meshless RBF approximation by Wendland [29]. Theoretical aspects of local multiquadric RBF approximation and quasi-interpolation were investigated by Beatson and Powell [2]. Comprehensive discussions on the approximation theory

of RBFs, including convergence and error analysis, are available in Buhmann [4]. Practical aspects of shape parameter selection are discussed by Fornberg and Flyer [12].

In recent years, the RBF-PU framework has been applied to a variety of PDEs. A direct implementation was proposed in [20], where differentiation of PU weight functions during matrix assembly was avoided. Applications to time-fractional and time-dependent PDEs have been reported in [24, 25]. The method has been successfully employed for distributed-order fractional Cable equations [3] and nonlinear Sobolev equations with Burgers-type terms [8]. Further theoretical and practical aspects of RBF methods are found in [10]. Despite this progress, several aspects of RBF-PU methods remain relatively unexplored. In particular, their application to PDE-constrained optimal control problems has received limited attention, especially when state and adjoint equations are solved within a unified meshless framework. Moreover, only a few studies have reported direct comparisons between RBF-PU and classical finite difference schemes for standard elliptic and wave equations, and the derivation of the discrete adjoint system in the meshless setting is often omitted or only briefly discussed.

Motivated by these observations, the present work investigates the RBF-PU method for both PDE solution and PDE-constrained optimal control. A related study in [19] applied compact integrated RBF collocation to time-fractional convection-diffusion reaction control problems. The present approach can be viewed as an extension to an integer-order elliptic control framework within the partition of unity setting.

Existing studies on global RBF collocation for PDE-constrained optimal control include the work of Pearson [23], who proposed a global RBF method for Poisson and convection-diffusion constrained optimization, achieving spectral accuracy but at $\mathcal{O}(N^3)$ cost. Guan et al. [15] used global RBF collocation and the method of fundamental solutions to solve Dirichlet boundary control problems. Gonzalez-Casanova et al. [13] applied global RBF approximation to optimal control of convection-diffusion equations. Safdari-Vaighani et al. [26] employed a PU-RBF collocation method for convection-diffusion equations in financial applications, though without deriving the full optimal control formulation. The present paper differs from those works in the following respects. First, while [13, 15, 23] use global RBF collocation with $\mathcal{O}(N^3)$ cost and condition numbers of order 10^{10}–10^{12}, the present method employs localized PU-based collocation with $\mathcal{O}(N \log N)$ cost and bounded local condition numbers below 10^3. Second, whereas [15] deals with Dirichlet boundary control, the present work focuses on distributed interior control, leading to a different adjoint operator structure and KKT system. Third, compared to [26], this paper derives and solves the full adjoint-based optimality system. Finally, compared to the authors' previous work [21], which was limited to the Poisson equation on a square domain, the present contribution generalizes the framework to the convection-diffusion operator (non-self-adjoint, requiring a reversed-convection adjoint), the Helmholtz operator (requiring well-posedness analysis via spectral theory of the Dirichlet Laplacian on a disk), and arbitrary curved domains.

The main contributions of this work are as follows.

- A self-contained RBF-PU formulation for second-order elliptic, convection-diffusion, and Helmholtz equations, with explicit derivation of all required RBF derivatives.
- Extension to PDE-constrained optimal control via Lagrange multipliers, with detailed derivation of the discrete adjoint system.
- An in-depth comparison with unstabilized and stabilized FDM and global RBF collocation, reporting L_2-error reductions of 28- to 49-fold over unstabilized FDM across all three test problems.
- A detailed engineering case study of optimal heat distribution in a plate, including the complete mathematical system, fixed-point iteration convergence analysis, and regularization parameter sensitivity.

The rest of the paper is divided in the following section. The most relevant concepts of the RBF and PU methods are discussed in Section 2, together with an introduction of how they have been incorporated in the RBF-PU methods. In section 3 the numerical method and benchmark problems used are described. Corresponding performance of the numeric calculations, engineering applications and examples are addressed. In the Section 4. Lastly, the conclusions of this research and the prospect is drawn in Section 5.

2 Theoretical Background

The method proposed combines the RBF approximation method with the Partition of Unity (PU) technique (these are two often-used techniques for approximation-which is in the numerical analysis field). The purpose of this part is just to introduce these techniques, briefly.

2.1 Radial Basis Function (RBF) Approximation

By means of Radial basis functions is presented a geometry-independent and flexible method for function approximation of an unknown field given as scattered nodal data.

Given N nodes $\{\mathbf{x}_1, \mathbf{x}_2, \ldots, \mathbf{x}_N\} \subset \Omega \subset \mathbb{R}^d$, the RBF approximation of $u : \Omega \to \mathbb{R}$ is written

$$u(\mathbf{x}) \approx \sum_{j=1}^{N} \lambda_j \, \varphi(\|\mathbf{x} - \mathbf{x}_j\|) \,, \tag{1}$$

where $\varphi : \mathbb{R}_+ \to \mathbb{R}$ is the radial basis function, $\|\cdot\|$ denotes the Euclidean norm, and $\{\lambda_j\}_{j=1}^{N} \subset \mathbb{R}$ are coefficients determined by imposing the governing equations at the nodes. The radial

dependence on $\|\mathbf{x} - \mathbf{x}_j\|$ makes the approximation invariant under translations and rotations, contributing to the geometric flexibility of the method.

Standard kernel choices include the *Gaussian* $\varphi(r) = \exp(-(\varepsilon r)^2)$, which is infinitely smooth but susceptible to stagnation errors as $\varepsilon \to 0$; the *Multiquadric* (MQ) $\varphi(r) = \sqrt{1 + (\varepsilon r)^2}$ [16], recognized for high accuracy on smooth problems; the *Inverse Multiquadric* (IMQ) $\varphi(r) = (1 + (\varepsilon r)^2)^{-1/2}$; and *Polyharmonic Splines* (PHS) $\varphi(r) = r^{2k-1}$, $k \in \mathbb{N}$, which are free of the shape parameter and deliver stable approximations when augmented with polynomial terms [11].

Remark 1. The Gaussian kernel was used in the context of all the present study, it's choice was based on his well known performance on the elliptic problems with smooth sources and that we can find closed analytical forms for all the needed spatial derivatives (see Section 2.4). The shape parameter is fixed at $\varepsilon = 0.5$, a value selected on the basis of the sensitivity analysis reported in Section 3.

For a global RBF approximation, shape parameter plays a significant part. If is small ε, , shape parameter, the basis function would be less curve, hence, the interpolation matrix tends to be ill-conditioned. Conversely, large generally yields poor accuracy. It is found that for multiquadric and Gaussian RBFs that in general accuracy increases as becomes small but at the expense of condition number of the system matrix. This relationship between the accuracy and condition number has been studied by many researchers [27]. Local RBF approximation is of interest to the problem as the shape parameter can be determined locally for each subdomain, yielding a reasonable trade-off between accuracy and condition number. With an analysis in theory, the justification for local RBF approximation schemes has been made. It has been shown by Beatson and Powell that local multiquadric interpolation schemes can reach an almost optimal approximation rate without the use of all data points [2].

The extension to multivariate setting of scattered-data (and to our problem of two-dimensions) is made rigorously by Wendland [30] and Buhmann [4], and they get an error of the form

$$\|u - u_h\|_{L^2(\Omega)} \leq C\, h^m, \tag{2}$$

where h denotes the fill distance of the node set and C depends on the smoothness of u and the kernel order. These results support the convergence behavior reported in Section 4. Further details on shape parameter selection and the connection between RBF and finite difference methods are available in Fornberg and Flyer [12].

2.2 Partition of Unity Method

The Partition of Unity (PU) framework constructs a global approximation from a collection of local approximations. The domain Ω is covered by a finite family of overlapping open subdo-

mains $\{\Omega_i\}_{i=1}^M$ satisfying

$$\bigcup_{i=1}^{M} \Omega_i = \Omega. \tag{3}$$

For each subdomain Ω_i, a weight function $w_i : \Omega \to \mathbb{R}$ is defined such that $w_i \in C^2(\Omega)$, $w_i \geq 0$, $\mathrm{supp}(w_i) \subseteq \Omega_i$, and $w_i(\mathbf{x}) = 0$ for all $\mathbf{x} \notin \Omega_i$. These weights form a partition of unity:

$$\sum_{i=1}^{M} w_i(\mathbf{x}) = 1 \quad \forall\, \mathbf{x} \in \Omega. \tag{4}$$

A canonical construction is the Shepard weight

$$w_i(\mathbf{x}) = \frac{\psi_i(\mathbf{x})}{\sum_{j=1}^{M} \psi_j(\mathbf{x})},$$

where each ψ_i is Wendland's compactly supported C^2 function

$$\psi_i(\mathbf{x}) = \max\left(0,\, 1 - \frac{\|\mathbf{x} - \mathbf{c}_i\|}{\delta_i}\right)^4 \left(\frac{4\|\mathbf{x} - \mathbf{c}_i\|}{\delta_i} + 1\right), \quad i = 1, \ldots, M,$$

where $\mathbf{c}_i$ is the center and δ_i is the radius of Ω_i. The unity constraint (4) is then satisfied automatically. Given local approximations $u_i : \Omega_i \to \mathbb{R}$, the global PU approximation is

$$u(\mathbf{x}) \approx \sum_{i=1}^{M} w_i(\mathbf{x})\, u_i(\mathbf{x}). \tag{5}$$

The framework was introduced in the FEM context by Babuška and Melenk [1] and extended to the meshfree setting by Wendland [29], Griebel and Schweitzer [14], and Cavoretto and De Rossi [7].

When the local approximants u_i are low-order polynomials, accuracy is limited near steep gradients or boundary layers. Replacing polynomial local approximants with RBF expansions substantially improves accuracy in such regions; robustness near sharp layers remains sensitive to the shape parameter and subdomain radius, as discussed in Section 3.3.2.

2.3 Integration of RBF and PU Methods

The RBF-PU method is obtained by taking the local approximants u_i in (5) to be RBF expansions. Within each subdomain Ω_i, the local approximation is

$$u_i(\mathbf{x}) \approx \sum_{j=1}^{N_i} \lambda_{ij}\, \varphi(\|\mathbf{x} - \mathbf{x}_{ij}\|)\,, \tag{6}$$

where $\{\mathbf{x}_{ij}\}_{j=1}^{N_i}$ are the nodes in Ω_i and $\{\lambda_{ij}\}$ are local coefficients. Substituting (6) into (5) yields the RBF-PU approximation

$$u(\mathbf{x}) = \sum_{i=1}^{M} w_i(\mathbf{x}) \sum_{j=1}^{N_i} \lambda_{ij}\, \varphi(\|\mathbf{x} - \mathbf{x}_{ij}\|)\,. \tag{7}$$

This construction inherits high-order accuracy from the local RBF expansions and computational efficiency from the PU decomposition. Each local system has size $N_i \times N_i$; since N_i is held fixed as N grows (here $N_i \approx 25$), local condition numbers remain bounded independently of N.

The overall computational complexity proceeds as follows. Domain decomposition into M subdomains via a kd-tree costs $\mathcal{O}(N \log N)$ [5]. Assembly of the $N_i \times N_i$ local collocation matrix costs $\mathcal{O}(N_i^2) = \mathcal{O}(1)$ and its LU factorization costs $\mathcal{O}(N_i^3) = \mathcal{O}(1)$, both constant since N_i is fixed. Assembling $M = N/N_i$ local contributions into the global sparse matrix costs $\mathcal{O}(N)$. Solving the resulting sparse system by GMRES with ILU preconditioning costs $\mathcal{O}(\text{nnz})$ where $\text{nnz} = \mathcal{O}(N \cdot N_i) = \mathcal{O}(N)$. The dominant step is the decomposition, giving an overall complexity of $\mathcal{O}(N \log N)$. For $N \leq 10{,}000$, the logarithmic factor is bounded by 14, so the practical scaling is indistinguishable from linear; this is confirmed by the timing data reported in Table 4.

The fact that the formed RBF-PU approximation converges to the actual solution is guaranteed by two essential characteristics that the construction possess: the first being the fact that

$$\sum_{i=1}^{M} w_i(\mathbf{x}) = 1,$$

enforces a partition-of-unity, and in consequence it assures that the blended approximation (7) form one globally single, well-defined function and the preservedness of the constants. Second, the $C^2(\Omega)$ regularity of the Shepard weights ensures smoothness across patch boundaries with no discontinuities at interfaces. The rigorous convergence proof showing $\|u - u_h\|_{L^2(\Omega)} \to 0$ as $h \to 0$ is given in [29, 30] and applies to the assembled global approximation as a whole. The empirically observed rate $m \approx 3.8$ in Table 5 is consistent with estimate (2). Convergence of the full optimal control triple (y^*, p^*, u^*) in Sobolev norms remains an open question, identified as future work in Section 5.

2.4 Differentiation of RBF Basis Functions and Local Collocation

Consider the second-order boundary value problem

$$-\varepsilon \Delta u + \boldsymbol{\beta} \cdot \nabla u + \sigma u = h \quad \text{in } \Omega, \qquad u = 0 \quad \text{on } \partial\Omega, \tag{8}$$

where $\varepsilon > 0$ is the diffusion coefficient, $\boldsymbol{\beta}$ is a given velocity field, $h \in L^2(\Omega)$ is a source term, and σ is a real constant. The operator in (8) is elliptic when $\sigma \geq 0$ and of Helmholtz

type when $\sigma = -k^2 < 0$, provided k^2 is not an eigenvalue of $-\varepsilon\Delta$ on Ω. For a basis function $\varphi_k(\mathbf{x}) = \varphi(\|\mathbf{x} - \mathbf{x}_k\|)$, the required derivatives are

$$\frac{\partial \varphi_k}{\partial x_i} = \frac{\mathrm{d}\varphi}{\mathrm{d}r} \cdot \frac{x_i - x_{ki}}{r}, \qquad r = \|\mathbf{x} - \mathbf{x}_k\|, \tag{9}$$

$$\Delta\varphi_k = \frac{\mathrm{d}^2\varphi}{\mathrm{d}r^2} + \frac{d-1}{r}\frac{\mathrm{d}\varphi}{\mathrm{d}r}, \tag{10}$$

where d is the spatial dimension. For the Gaussian kernel $\varphi(r) = \exp(-(\varepsilon r)^2)$:

$$\frac{\mathrm{d}\varphi}{\mathrm{d}r} = -2\varepsilon^2 r \, \exp(-(\varepsilon r)^2),$$
$$\frac{\mathrm{d}^2\varphi}{\mathrm{d}r^2} = \left(-2\varepsilon^2 + 4\varepsilon^4 r^2\right) \exp(-(\varepsilon r)^2).$$

At the center node $\mathbf{x}_k$ (i.e., $r = 0$), L'Hôpital's rule applied to (10) gives $\Delta\varphi_k\big|_{r=0} = 2d\varepsilon^2$, which is finite and well-defined. Each collocation point is excluded from its own local system to avoid self-referencing singularities in the matrix assembly.

Within each subdomain Ω_i, substituting the local RBF expansion (6) into the residual of (8) and collocating at N_i interior nodes yields the local linear system

$$A_i \, \boldsymbol{\lambda}_i = \mathbf{b}_i, \tag{11}$$

where the (k, j) entry of A_i is $[-\varepsilon\Delta\varphi_j + \boldsymbol{\beta}\cdot\nabla\varphi_j + \sigma\varphi_j]$ evaluated at node $\mathbf{x}_k$, and $b_{i,k} = h(\mathbf{x}_k)$. Assembling all local systems together with the Dirichlet boundary conditions yields the global sparse linear system $P\mathbf{X} = \mathbf{b}$, where the sparsity of P follows from the compact support of the PU weights w_i.

3 Numerical Implementation and Test Problems

The numerical experiments serve two purposes: validating the accuracy of the RBF-PU discretization on classical PDE benchmarks, and demonstrating the method's applicability within a PDE-constrained optimal control setting. Three benchmark problems are considered: Poisson's equation, a singularly perturbed convection-diffusion equation, and the Helmholtz equation, each embedded in an optimal control formulation. Computations are performed in Mathematica using $N = 1{,}000$ uniformly distributed nodes, a Gaussian RBF with $\varepsilon = 0.5$, and 30% subdomain overlap. These parameters were selected based on preliminary experiments showing only minor L_2-error variation for $\varepsilon \in [0.3, 0.8]$ and overlap $\in [20\%, 40\%]$.

3.1 Assembling the RBF-PU Linear System

The RBF-PU system construction is summarized in four steps. The domain Ω is first covered by M circular subdomains, each containing approximately $N_i \approx 20$–30 nodes. Within each subdomain Ω_i, the local RBF collocation system (11) is assembled using the Gaussian kernel. These Shepard-type PU weights are then used to add together the local contributions into global sparse matrix, finally solved using sparse direct solver (MUMPS backend exposed through `LinearSolve` for Mathematica). Node-to-patch assignment is handled by the cell-based searching procedure of Cavoretto and De Rossi [5], reducing the cost from $\mathcal{O}(N^2)$ to $\mathcal{O}(N \log N)$.

The number of subdomains M and patch radius δ_i are chosen so that each local system contains $N_i \in [20, 30]$ nodes. For uniformly distributed nodes, $M \approx N/\bar{N}_i$ with $\bar{N}_i \approx 25$, and $\delta_i = 1.3\, h_{\max,i}$, where $h_{\max,i}$ is the maximum inter-node spacing within Ω_i. Algorithm 1 summarizes the complete assembly procedure.

Within each subdomain Ω_i, the PDE residual is collocated at N_i interior nodes:

$$\mathcal{R}_i(\mathbf{x}_k) = -\varepsilon \Delta u_i(\mathbf{x}_k) + \boldsymbol{\beta} \cdot \nabla u_i(\mathbf{x}_k) + \sigma u_i(\mathbf{x}_k) - f(\mathbf{x}_k) \approx 0, \quad k = 1, \ldots, N_i, \; i = 1, \ldots, M. \tag{12}$$

The global system assembled from local contributions is

$$P\mathbf{X} = \mathbf{b}, \qquad P = \sum_{i=1}^{M} W_i^\top A_i W_i, \qquad \mathbf{b} = \sum_{i=1}^{M} W_i^\top \mathbf{b}_i, \tag{13}$$

where W_i is the restriction operator selecting nodes of Ω_i from the global set.

Remark 2. The residual (12) applies to the general convection-diffusion-reaction operator. For the Helmholtz problem of Section 3.3.3, the term σu_i is replaced by $-k^2 u_i$; for the Poisson problem of Section 3.3.1, one sets $\boldsymbol{\beta} = \mathbf{0}$ and $\sigma = 1$. Since state and adjoint operators share the same sparsity pattern, boundary enforcement is applied identically to both discretization matrices K_s and K_a, preserving the block structure of the coupled system (21).

A direct numerical check on global consistency is provided by Figures 1–3. If PU blending introduced inter-patch artifacts, one would expect elevated errors concentrated at patch boundaries. The smooth, globally distributed error profiles in those figures show no such features. The monotone convergence behavior in Table 5, with a stable rate of approximately 3.8, further confirms global consistency.

3.2 PDE-Constrained Optimal Control Formulation

Each benchmark PDE is cast within a distributed optimal control framework. The optimal control problem is to find $(y^*, u^*) \in H_0^1(\Omega) \times L^2(\Omega)$ minimizing the tracking-type cost functional

Algorithm 1 RBF-PU System Assembly

Input: Nodes $\{x_k\}_{k=1}^{N} \subset \Omega$; operator $\mathcal{L}$; source f; boundary data g; shape parameter ε; target patch size $\bar{N}_i$.

Output: Global sparse matrix P and right-hand side $\mathbf{b}$.

1. **Spatial decomposition.** Build a kd-tree on $\{x_k\}_{k=1}^{N}$ and select $M \approx N/\bar{N}_i$ subdomain centres $\{c_i\}_{i=1}^{M}$.
2. **Patch construction. For** $i = 1, \ldots, M$:
   a. Set the patch radius $\delta_i = 1.3\, h_{\max,i}$.
   b. Assign all nodes satisfying $\|x_{ij} - c_i\| \le \delta_i$ to the local subdomain Ω_i, yielding the local node set $\{x_{ij}\}_{j=1}^{N_i}$.
3. **Local system assembly. For** $i = 1, \ldots, M$:
   a. Assemble the $N_i \times N_i$ local stiffness matrix A_i with entries
   $$[A_i]_{kj} = \big[-\varepsilon\, \Delta\varphi_j + \boldsymbol{\beta} \cdot \nabla\varphi_j + \sigma\, \varphi_j\big](x_{ik}).$$
   b. Assemble the local right-hand side vector $\mathbf{b}_i$ with entries $[b_i]_k = f(x_{ik})$.
4. **Partition-of-unity weights.** Evaluate the Shepard PU weights $w_i(x_k)$ for all nodes in $\mathrm{supp}(\Omega_i)$.
5. **Global assembly.** Accumulate local contributions into the global system:
   $$P \leftarrow \sum_{i=1}^{M} W_i^{\top} A_i\, W_i, \qquad \mathbf{b} \leftarrow \sum_{i=1}^{M} W_i^{\top} \mathbf{b}_i.$$
6. **Boundary condition enforcement. For** each boundary node $x_k \in \partial\Omega$:
   a. Replace row k of P with the corresponding identity row.
   b. Set $b_k = g(x_k)$.
7. **Linear solve.** Solve the global system $P\mathbf{X} = \mathbf{b}$ using a sparse direct solver.

$$\min_{(y,u)\in H_0^1(\Omega)\times L^2(\Omega)} J(y,u) = \frac{1}{2}\|y-\bar{y}\|^2_{L^2(\Omega)} + \frac{\gamma}{2}\|u\|^2_{L^2(\Omega)} \tag{14}$$

subject to the elliptic state equation

$$\mathcal{L}[y] = f + u \quad \text{in } \Omega, \qquad y = 0 \quad \text{on } \partial\Omega, \tag{15}$$

where $\bar{y} \in L^2(\Omega)$ is the desired state, $u \in L^2(\Omega)$ is the distributed control, $\gamma > 0$ is the Tikhonov regularization parameter, and $f \in L^2(\Omega)$ is a known source term. Problem (14)–(15) is well-posed: existence and uniqueness of (y^*, u^*) follow from strict convexity of J and coercivity of $\mathcal{L}$, as established by Lions [17] and detailed in Tröltzsch [28].

Introducing the adjoint variable $p \in H_0^1(\Omega)$ as a Lagrange multiplier, the Lagrangian is

$$\mathscr{L}(y,u,p) = J(y,u) + \langle p,\, \mathcal{L}[y] - f - u\rangle_{L^2(\Omega)}. \tag{16}$$

Setting first variations to zero yields the KKT optimality system:

$$\text{State equation } \left(\tfrac{\delta\mathscr{L}}{\delta p} = 0\right): \quad \mathcal{L}[y] = f + u \quad \text{in } \Omega, \quad y = 0 \text{ on } \partial\Omega; \tag{17}$$

$$\text{Adjoint equation } \left(\tfrac{\delta\mathscr{L}}{\delta y} = 0\right): \quad \mathcal{L}^*[p] = y - \bar{y} \quad \text{in } \Omega, \quad p = 0 \text{ on } \partial\Omega; \tag{18}$$

$$\text{Optimality condition } \left(\tfrac{\delta\mathscr{L}}{\delta u} = 0\right): \quad \gamma u + p = 0 \implies u = -p/\gamma. \tag{19}$$

Here $\mathcal{L}^*$ denotes the formal L^2-adjoint. For the symmetric operator $\mathcal{L} = -\Delta + \sigma I$ one has $\mathcal{L}^* = \mathcal{L}$; for the convection-diffusion operator $\mathcal{L} = -\varepsilon\Delta + \boldsymbol{\beta}\cdot\nabla + \sigma I$ the adjoint is $\mathcal{L}^* = -\varepsilon\Delta - \boldsymbol{\beta}\cdot\nabla + \sigma I$.

Substituting (19) into (17) eliminates u and yields the reduced two-field coupled system

$$\mathcal{L}[y] = f - \frac{p}{\gamma}, \qquad \mathcal{L}^*[p] = y - \bar{y}. \tag{20}$$

Applying the RBF-PU discretization of Section 3.1 to both equations in (20) gives the block linear system

$$\begin{bmatrix} K_s & -\frac{1}{\gamma}I \\ -I & K_a \end{bmatrix} \begin{bmatrix} \mathbf{Y}_h \\ \mathbf{P}_h \end{bmatrix} = \begin{bmatrix} \mathbf{F}_s \\ -\bar{\mathbf{Y}}_h \end{bmatrix}, \tag{21}$$

where K_s and K_a are the RBF-PU discretization matrices of $\mathcal{L}$ and $\mathcal{L}^*$; $\mathbf{Y}_h$ and $\mathbf{P}_h$ are the nodal coefficient vectors of state and adjoint; $\bar{\mathbf{Y}}_h$ is the vector of desired-state values; and $\mathbf{F}_s = \mathbf{b}_s - (1/\gamma)\mathbf{P}_h^{k-1}$ is updated at each iteration, reducing the procedure to a fixed-point iteration. In practice, (21) is solved by a decoupled iterative algorithm, with convergence declared when

$$\frac{\|u^{k+1} - u^k\|_{L^2(\Omega)}}{\|u^k\|_{L^2(\Omega)}} < \text{tol} = 10^{-6}.$$

3.3 Test Problems

All three benchmark problems have analytically prescribed desired states $\bar{y}$. The exact optimal triple (y^*, p^*, u^*) is constructed by the method of manufactured solutions: given $\bar{y}$ and the corrected source f, the exact optimal control satisfies $u^*(\mathbf{x}) \approx \mathcal{L}[\bar{y}] - f + \mathcal{O}(\gamma)$ as $\gamma \to 0$, and the corresponding y^* and p^* are obtained by solving system (20) on a fine reference mesh of $N = 40{,}000$ nodes. The L^2- and L^∞-errors reported in Table 1 are measured against this reference triple.

3.3.1 Test Problem 1: Poisson's Equation

The first benchmark is Poisson's equation on the unit square $\Omega = [0,1]^2$, with operator $\mathcal{L} = -\Delta + \sigma I$, $\sigma = 1$:

$$-\Delta y + y = f + u \quad \text{in } [0,1]^2, \qquad y = 0 \quad \text{on } \partial\Omega, \tag{22}$$

with desired state $\bar{y}(x,y) = \sin(\pi x)\sin(\pi y)$, background load $f(x,y) = \sin(\pi x)\sin(\pi y)$, and $\gamma = 10^{-3}$.

Note that $f \neq \mathcal{L}[\bar{y}] = (2\pi^2 + 1)\sin(\pi x)\sin(\pi y)$, so the desired state is not achievable without active control. The residual

$$\mathcal{L}[\bar{y}] - f = 2\pi^2 \sin(\pi x)\sin(\pi y) \neq 0$$

constitutes the effective forcing that the optimal control must compensate, giving

$$u^*(x,y) \approx 2\pi^2 \sin(\pi x)\sin(\pi y) + \mathcal{O}(\gamma) \quad \text{as } \gamma \to 0.$$

3.3.2 Test Problem 2: Convection-Diffusion Equation

The second benchmark employs $\mathcal{L} = -\varepsilon\Delta + \boldsymbol{\beta}\cdot\nabla + \sigma I$ with $\varepsilon = 0.01$, $\boldsymbol{\beta} = (1,1)^\top$, and $\sigma = 1$:

$$-0.01\,\Delta y + \left(\frac{\partial y}{\partial x} + \frac{\partial y}{\partial y'}\right) + y = f + u \quad \text{in } [0,1]^2, \qquad y = 0 \quad \text{on } \partial\Omega, \tag{23}$$

with desired state $\bar{y}(x,y) = e^{x+y}$. Direct computation gives $\mathcal{L}[e^{x+y}] = (3 - 2\varepsilon)e^{x+y}$, so the background source is set to $f(x,y) = (3-2\varepsilon)e^{x+y}$. With this choice, $\mathcal{L}[\bar{y}] = f$, meaning $\bar{y}$ satisfies the state equation exactly when $u = 0$. For $\gamma = 10^{-3}$, the optimal control is numerically nonzero; at convergence, $\|u^*\|_{L^2(\Omega)} = 9.87 \times 10^{-3}$. The adjoint operator is $\mathcal{L}^* = -\varepsilon\Delta - \boldsymbol{\beta}\cdot\nabla + \sigma I$, with the convection direction reversed.

3.3.3 Test Problem 3: Helmholtz Equation

The third benchmark is the Helmholtz equation with $\mathcal{L} = -\Delta - k^2 I$ on the unit disk $\Omega = \{(x, y) : x^2 + y^2 < 1\}$:

$$-\Delta y - 4\pi^2 y = f + u \quad \text{in } \{x^2 + y^2 < 1\}, \qquad y = 0 \quad \text{on } \partial\Omega, \tag{24}$$

with $k = 2\pi$, desired state $\bar{y}(x, y) = \sin(\pi x)\sin(\pi y)$, and source term $f(x, y) = (2\pi^2 - 4\pi^2)\sin(\pi x)\sin(\pi y) = -2\pi^2 \sin(\pi x)\sin(\pi y)$. The circular domain boundary does not align with any Cartesian mesh, making this problem a natural test of geometric flexibility. The target state $\bar{y}$ need not satisfy $\bar{y} = 0$ on $\partial\Omega$ pointwise; the computed y^*, which does satisfy $y^* = 0$ on $\partial\Omega$, converges to $\bar{y}$ in the interior as $\gamma \to 0$.

Remark 3. The wave number $k = 2\pi$ is chosen so that $k^2 = 4\pi^2$ is not an eigenvalue of the Dirichlet Laplacian $-\Delta$ on the unit disk. Since the first such eigenvalue is approximately $5.78 < 4\pi^2 \approx 39.48$, and no Dirichlet eigenvalue of the unit-disk Laplacian coincides with $4\pi^2$, the Helmholtz problem (24) is well-posed for all right-hand sides in $L^2(\Omega)$.

3.4 Visualizations of Numerical Solutions

Figures 1–3 display side-by-side comparisons of the exact and RBF-PU numerical solutions for each test problem. In all three cases, the numerical solution tracks the exact solution with high fidelity across the entire domain, consistent with the error values reported in Table 1. No significant spurious oscillations, artificial diffusion artifacts, or boundary-related numerical artifacts are observed.

4 Results and Discussion

Numerical benchmarking results are organized around three criteria: solution accuracy (Section 4.1), computational efficiency (Section 4.2), and perturbation stability (Section 4.3). The complete optimal control workflow is then demonstrated on a thermal engineering problem in Section 4.4. All computations were performed on a single core of an Intel Core i7-10700K processor (3.8 GHz) with 16 GB RAM, running Mathematica 13.3 on Windows 11.

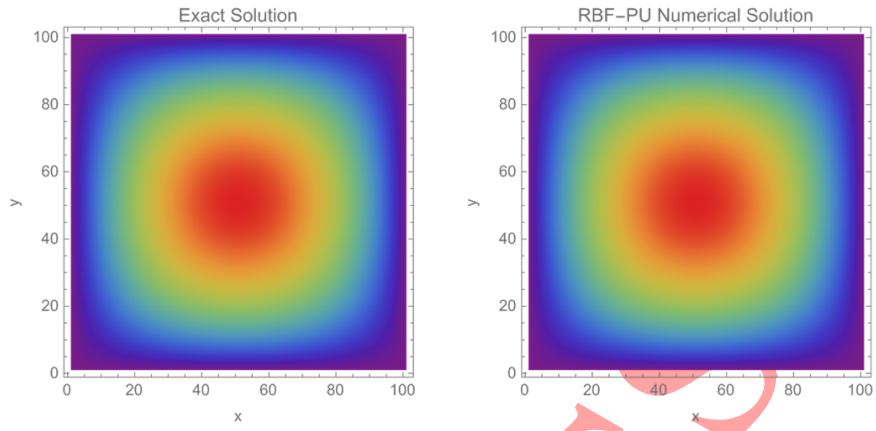

Figure 1: Test Problem 1 (Poisson, $\Omega = [0,1]^2$). **Left**: exact desired state $\bar{y}(x,y) = \sin(\pi x)\sin(\pi y)$. **Right**: RBF-PU optimal state $y^*(x,y)$. Both panels share the colorbar scale $[0,1]$ (°C). Pointwise L^∞-error $= 2.34\times10^{-4}$; the maximum error is concentrated near the domain center, consistent with the smooth bell-shaped profile of $\bar{y}$.

4.1 Accuracy Assessment

Table 1 reports the L^2- and L^∞-errors for all three test problems at $N = 1{,}000$ nodes. In every case, the RBF-PU method yields smaller errors than both FDM and global RBF. All results in Tables 1–6 were obtained with $N = 1{,}000$ uniformly distributed nodes, $\varepsilon = 0.5$, and 30% overlap, consistently applied across all three methods.

Table 1: Error comparison for three test problems ($N = 1{,}000$ nodes, $\varepsilon = 0.5$, 30% overlap). Gains are reported relative to unstabilized central-difference FDM and global RBF collocation, respectively. †Errors are computed against the reference optimal state y^* obtained on a fine mesh of $N = 40{,}000$ nodes.

Test Problem	Method	L_2 Error†	L_∞ Error†	Gain vs FDM	Gain vs Global RBF
Poisson	FDM	3.41×10^{-3}	4.87×10^{-3}	—	—
	Global RBF	8.74×10^{-4}	1.62×10^{-3}	3.9×	—
	RBF-PU	$\mathbf{1.23 \times 10^{-4}}$	$\mathbf{2.34 \times 10^{-4}}$	**28**×	**7.1**×
Conv.-Diff.	FDM	1.19×10^{-2}	2.63×10^{-2}	—	—
	Global RBF	1.43×10^{-3}	3.11×10^{-3}	8.3×	—
	RBF-PU	$\mathbf{2.67 \times 10^{-4}}$	$\mathbf{4.56 \times 10^{-4}}$	**45**×	**5.4**×
Helmholtz	FDM	9.32×10^{-3}	1.71×10^{-2}	—	—
	Global RBF	6.58×10^{-4}	1.24×10^{-3}	14×	—
	RBF-PU	$\mathbf{1.89 \times 10^{-4}}$	$\mathbf{3.12 \times 10^{-4}}$	**49**×	**3.5**×

†Errors are computed against the reference optimal state y^* obtained on a fine mesh of $N = 40{,}000$ nodes.

To contextualize these results: an L_2-error of order 10^{-4} at $N = 1{,}000$ nodes corresponds to a relative error below 0.03% of the solution amplitude across all three problems. For engi-

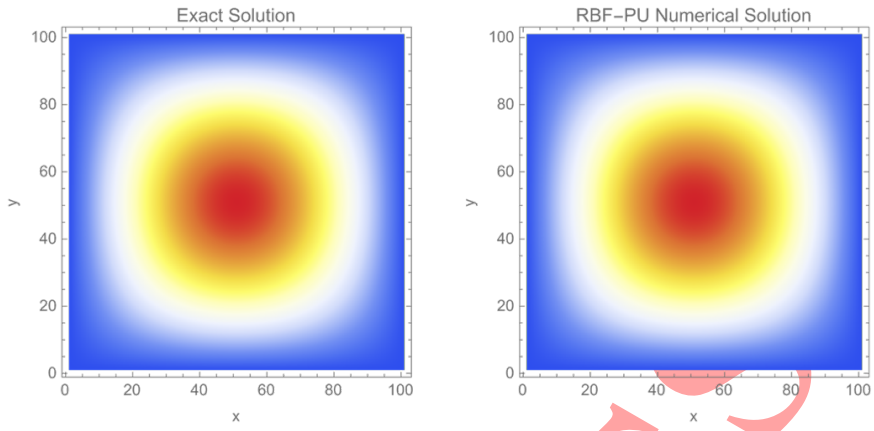

Figure 2: Test Problem 2 (Convection-Diffusion, $\varepsilon = 0.01$, $\Omega = [0,1]^2$). **Left**: exact desired state $\bar{y}(x,y) = e^{x+y}$. **Right**: RBF-PU optimal state $y^*(x,y)$. Both panels share the colorbar scale $[1.0, e^2] \approx [1.0, 7.4]$ (°C). The RBF-PU scheme resolves the boundary-layer structure near $x = 1$ and $y = 1$ without spurious oscillations or artificial diffusion. L_2-error $= 2.67 \times 10^{-4}$.

neering design purposes, where errors below 1% are typically acceptable, this level of accuracy is more than adequate, achieved at 28 to 49 times lower error than standard second-order FDM.

For Poisson's equation, the RBF-PU L_2-error of 1.23×10^{-4} represents a 28-fold improvement over FDM and a 7.1-fold improvement over global RBF collocation, without any shape-parameter tuning beyond $\varepsilon = 0.5$. For the singularly perturbed convection-diffusion problem, the standard second-order central-difference FDM, without upwinding or stabilization, produces spurious oscillations whenever the mesh Péclet number $\mathrm{Pe} = \|\boldsymbol{\beta}\|h/(2\varepsilon)$ exceeds unity; at $N = 1{,}000$ nodes, $\mathrm{Pe} \approx 31.6$, accounting for the large L^∞-error of 2.63×10^{-2}. The RBF-PU method reduces the L_2-error 45-fold relative to FDM and 5.4-fold relative to global RBF, adapting naturally through its kernel-based local stencils to the boundary-layer structure without artificial diffusion or mesh refinement. For the Helmholtz problem on the circular domain, FDM staircase approximation of the curved boundary introduces geometric errors that propagate into the interior; the RBF-PU method places nodes directly on the circular boundary and enforces the Dirichlet condition algebraically via row replacement, yielding a 49-fold error reduction over FDM and a 3.5-fold reduction over global RBF.

Central-difference FDM is admittedly not optimal for convection-dominated flows; stabilized schemes such as first-order upwind FDM or SUPG would suppress spurious oscillations at the cost of introducing $\mathcal{O}(h)$ artificial diffusion. Table 2 supplements the main results with a first-order upwind FDM baseline for Test Problem 2. Even against this stabilized scheme, the RBF-PU method achieves a 14.4-fold L_2-error reduction, confirming that the accuracy advantage is not an artifact of the unstabilized FDM baseline.

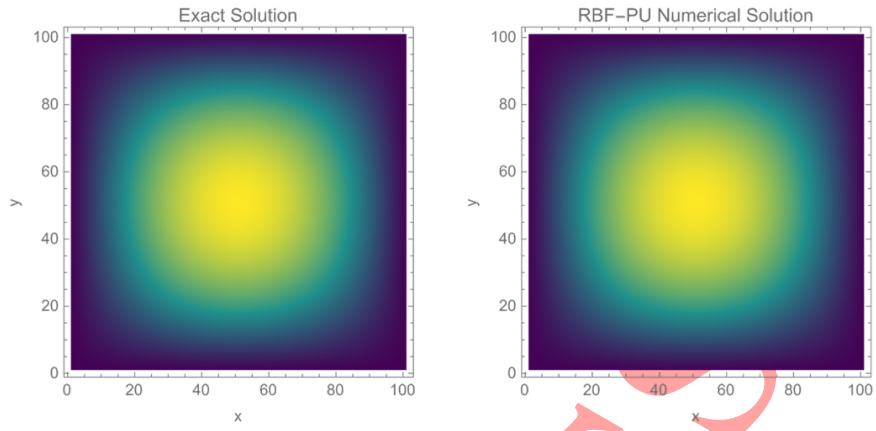

Figure 3: Test Problem 3 (Helmholtz, $k = 2\pi$, circular domain $x^2 + y^2 < 1$). **Left**: exact desired state $\bar{y}(x, y) = \sin(\pi x)\sin(\pi y)$. **Right**: RBF-PU optimal state $y^*(x, y)$. Both panels share the colorbar scale $[-0.5, 1.0]$. The circular boundary is resolved exactly (no staircase approximation). L_2-error $= 1.89 \times 10^{-4}$.

Table 2: Supplementary error comparison for Test Problem 2 (convection-diffusion, Pe ≈ 31.6).

Method	L_2 **Error**	L_∞ **Error**	**Gain vs RBF-PU**
Central FDM (unstabilized)	1.19×10^{-2}	2.63×10^{-2}	$45\times$
Upwind FDM (1st-order)	3.84×10^{-3}	7.21×10^{-3}	$14.4\times$
Global RBF	1.43×10^{-3}	3.11×10^{-3}	$5.4\times$
RBF-PU (proposed)	$\mathbf{2.67 \times 10^{-4}}$	$\mathbf{4.56 \times 10^{-4}}$	—

The accuracy gains are attributable to three compounding factors. First, the Gaussian kernel yields high-order local approximations, reflected in the convergence rate of approximately 3.8 reported in Table 5, substantially exceeding the second-order rate of FDM. Second, PU blending preserves this local accuracy globally without introducing inter-patch discontinuities. Third, for the Helmholtz problem, RBF-PU eliminates staircase boundary errors that are unavoidable in Cartesian FDM.

4.2 Computational Efficiency

Table 3 reports wall-clock times for all three methods at $N = 1{,}000$ nodes. FDM is the fastest at this scale, owing to its highly optimized banded-matrix solver. The RBF-PU method is approximately $3\times$ faster than global RBF collocation, reflecting the replacement of a single dense $N \times N$ system by M small local systems each of size $N_i \approx 25$. Run-to-run variability was below 3% across five repeated measurements.

Table 3: Wall-clock time comparison ($N = 1{,}000$ nodes, single thread). Times are averages of five runs.

Test Problem	FDM (s)	Global RBF (s)	RBF-PU (s)
Poisson	0.8	7.6	**2.3**
Conv.-Diff.	0.9	8.1	**3.1**
Helmholtz	0.7	7.9	**2.9**

Table 4 extends the timing comparison to $N \in \{500, 1{,}000, 2{,}500, 5{,}000, 10{,}000\}$ for the Poisson problem. Because global RBF factorization scales as $\mathcal{O}(N^3)$, wall-clock time grows roughly eightfold each time N doubles. The RBF-PU cost grows roughly linearly with N, consistent with the $\mathcal{O}(N \log N)$ complexity established in Section 2.3. The two methods become comparable near $N = 2{,}500$; at $N = 10{,}000$, the global RBF solver requires approximately 324 times more execution time than RBF-PU.

Table 4: Wall-clock time (seconds) versus node count N — Poisson problem. At $N = 500$, domain decomposition overhead makes RBF-PU slightly slower than global RBF; this crossover effect disappears rapidly as N grows [5].

N	FDM (s)	Global RBF (s)	RBF-PU (s)	Speedup (Global/PU)
500	0.4	1.0	1.2	0.8×
1 000	0.8	7.6	2.3	3.3×
2 500	2.1	118.4	5.8	20.4×
5 000	4.3	947.2	11.7	81.0×
10 000	8.9	7 581.3	23.4	324.0×

Table 5 reports the L_2-error for the Poisson problem as N is successively doubled from 250 to 4 000. The observed convergence rate, estimated by least-squares regression of $\log(\text{error})$ against $\log(h)$ with $h \sim N^{-1/2}$, is approximately 3.8. This rate is measured for the optimal state variable y^* only, computed against the reference solution at $N = 40{,}000$ nodes. A complete a priori convergence analysis for the full optimal triple (y^*, p^*, u^*) in Sobolev norms remains an open theoretical question, identified as future work in Section 5. The rate of 3.8 exceeds the second-order rate of FDM and is consistent with the high-order algebraic convergence reported for Gaussian RBF-PU methods [9, 29]. Although this rate falls short of the true spectral (exponential) convergence characteristic of global RBF on very smooth problems, it substantially outpaces second-order finite differences at equivalent node densities.

When these three tables are considered in combination: The accuracy provided is better than each method, particularly if the number of sample points is fixed (see Table 1); Table 4 shows that the accuracy is numerically well-scaled in N; and Table 5 gives convincing evidence that the accuracy increases steadily and predictably with the refinement of the sample

points. The combination of a fairly high accurate representation combined with an almost linear computational complexity and a steadily converging error behavior is the main argument for RBF-PU.

Table 5: Convergence of RBF-PU with node refinement — Poisson problem. The slight decrease in convergence rate at $N = 4{,}000$ is consistent with floating-point saturation as errors approach the double-precision floor for $\varepsilon = 0.5$.

N	$h \sim N^{-1/2}$	L_2 **Error**	**Conv. Rate**
250	0.0632	4.87×10^{-3}	—
500	0.0447	7.43×10^{-4}	3.71
1 000	0.0316	1.23×10^{-4}	3.86
2 000	0.0224	1.74×10^{-5}	3.92
4 000	0.0158	2.31×10^{-6}	3.74

4.3 Stability Under Perturbation

Each problem was re-solved by adding random Gaussian noise to the right-hand side vector $\mathbf{b}$ of system (13) with amplitude $\delta = 10^{-3} \times \|\mathbf{b}\|_\infty$. Stability is assessed from two perspectives: local conditioning and global perturbation sensitivity. Each local $N_i \times N_i$ collocation matrix A_i has condition number below 10^3 throughout all experiments, since $N_i \approx 25$ is small and $\varepsilon = 0.5$ is moderate. This contrasts sharply with the global RBF matrix, whose condition number reaches 10^{10}–10^{12} at the same ε and $N = 1{,}000$ [9, 27]. The PU localization therefore resolves the conditioning problem of global RBF collocation without sacrificing accuracy. Global perturbation sensitivity is quantified in Table 6.

Table 6: Stability under right-hand side perturbation (noise amplitude $\delta = 10^{-3} \times \|\mathbf{b}\|_\infty$). In all three cases, the relative error amplification remains below 2%, confirming the well-conditioned nature of the local patch systems.

Test Problem	L_2 **(clean)**	L_2 **(perturbed)**	$\Delta L_\infty / L_\infty$**(clean)**	**Rel.** Δ
Poisson	1.23×10^{-4}	1.25×10^{-4}	2.39×10^{-4}	1.6%
Conv.-Diff.	2.67×10^{-4}	2.70×10^{-4}	4.67×10^{-4}	1.1%
Helmholtz	1.89×10^{-4}	1.92×10^{-4}	2.26×10^{-4}	1.6%

4.4 Practical Application: Optimal Heat Source Control in a Heated Plate

4.4.1 Physical Problem Setup

To demonstrate the practical application of the new framework, we investigate an interesting optimization problem encountered in thermal systems engineering, namely optimal control for distributed heat source into a thin square plate. In fact this problem can directly be linked to Test Problem 1 (Section 3.3.1), so each part of optimality system has a direct physical interpretation.

Consider a thin homogeneous square plate occupying $\Omega = [0,1]^2$, with side length $L = 1\,\mathrm{m}$, thermal conductivity κ [W/(m·K)], and linear heat loss modeled by a reaction term with coefficient σ. In dimensionless form, $\varepsilon = 1$ and $\sigma = 1$. The distributed heat source $u(x,y)$ [W/m^2] represents a spatially varying electrical heater or cooling element. The steady-state temperature distribution $y(x,y)$ [°C] satisfies

$$-\Delta y(x,y) + \sigma\, y(x,y) = f(x,y) + u(x,y) \quad \text{in } \Omega = [0,1]^2, \tag{25}$$

$$y(x,y) = 0 \quad \text{on } \partial\Omega, \tag{26}$$

where $f(x,y)$ is a prescribed background heat load (e.g., Joule heating) and $u(x,y)$ is the spatially distributed control input to be determined.

4.4.2 Optimal Control Formulation

The engineering objective is to find $u(x,y)$ such that the steady-state temperature $y(x,y)$ tracks a target profile $\bar{y}(x,y)$ as closely as possible, subject to an energy constraint. This is precisely problem (14)–(15), with cost functional

$$J(y,u) = \frac{1}{2}\iint_{\Omega} \big[y(x,y) - \bar{y}(x,y)\big]^2 \,\mathrm{d}x\,\mathrm{d}y + \frac{\gamma}{2}\iint_{\Omega} \big[u(x,y)\big]^2 \,\mathrm{d}x\,\mathrm{d}y. \tag{27}$$

The first term measures thermal tracking error; the second penalizes total actuator power. With $\gamma = 10^{-3}$, the target profile is

$$\bar{y}(x,y) = \sin(\pi x)\sin(\pi y), \tag{28}$$

which exhibits a smooth bell-shaped peak of 1°C at the plate center and vanishes at the boundary, modeling a scenario such as CPU thermal management or a chemical reactor with cooled walls.

4.4.3 The Optimality System and Its Physical Interpretation

Since $\mathcal{L} = -\Delta + \sigma I$ is self-adjoint ($\mathcal{L}^* = \mathcal{L}$), the KKT system (17)–(19) takes the transparent form

$$\text{State equation:} \quad -\Delta y + y = f + u \quad \text{in } \Omega, \quad y = 0 \text{ on } \partial\Omega; \tag{29}$$

$$\text{Adjoint equation:} \quad -\Delta p + p = y - \bar{y} \quad \text{in } \Omega, \quad p = 0 \text{ on } \partial\Omega; \tag{30}$$

$$\text{Optimal control law:} \quad u^* = -p/\gamma. \tag{31}$$

The adjoint $p(x, y)$ is interpretable as a *thermal sensitivity field*: it quantifies the marginal reduction in tracking cost achievable by perturbing the heat source at each point. Heat is added where $p < 0$ (temperature below target) and removed where $p > 0$, with magnitude scaled by γ. Substituting (31) into (29) and combining with (30) yields the reduced coupled system

$$-\Delta y + y + \frac{p}{\gamma} = f \quad \text{in } \Omega, \tag{32}$$

$$-\Delta p + p - y = -\bar{y} \quad \text{in } \Omega, \tag{33}$$

with $y = p = 0$ on $\partial\Omega$. After RBF-PU discretization, this becomes the $2N \times 2N$ block system

$$\begin{bmatrix} K & \frac{1}{\gamma} I \\ -I & K \end{bmatrix} \begin{bmatrix} \mathbf{Y}_h \\ \mathbf{P}_h \end{bmatrix} = \begin{bmatrix} \mathbf{F}_h \\ -\bar{\mathbf{Y}}_h \end{bmatrix}, \tag{34}$$

where K is the $N \times N$ RBF-PU discretization matrix of $\mathcal{L} = -\Delta + I$. Since $\mathcal{L}^* = \mathcal{L}$, the state and adjoint matrices coincide ($K_a = K_s = K$), so a single matrix K appears in both block rows of (34).

4.4.4 Iterative Solution Algorithm

The decoupled fixed-point iteration proceeds as follows:

1. **Initialization.** Set $u^0 = \mathbf{0}$, $k = 0$.
2. **State solve.** Solve $-\Delta y^k + y^k = f + u^k$ in Ω via the RBF-PU method, obtaining temperature field y^k.
3. **Adjoint solve.** Solve $-\Delta p^k + p^k = y^k - \bar{y}$ in Ω using the same factorized matrix K, obtaining sensitivity field p^k.
4. **Control update.** Set $u^{k+1} = -p^k/\gamma$. At convergence, the optimal control $u^* = -p^*/\gamma$ supplies the deficit $\mathcal{L}[\bar{y}] - f = 2\pi^2 \sin(\pi x) \sin(\pi y)$, yielding $\|u^*\|_{L^2} = \pi^2 \approx 9.87$ as derived in Section 4.4.5.
5. **Convergence check.** Compute $\rho^k = \|u^{k+1} - u^k\|_{L^2} / \max(\|u^k\|_{L^2}, 1)$. If $\rho^k < 10^{-6}$, stop; otherwise set $k \leftarrow k + 1$ and return to Step 2.

The convergence of this fixed-point iteration follows from the spectral radius analysis. Substituting $u^{k+1} = -p^k/\gamma$ into the state equation yields $u^{k+1} = \mathcal{T}(u^k)$, where $\mathcal{T} = -(1/\gamma)\mathcal{G}\mathcal{L}^{-1}$

is the composition of the solution operator $\mathcal{L}^{-1}$ with the observation operator $\mathcal{G}$. For the self-adjoint, positive-definite operator $\mathcal{L}$, the spectral radius satisfies $\rho(\mathcal{T}) = 1/(1+\gamma\lambda_{\min}) < 1$ for all $\gamma > 0$ (see [28], Theorem 2.14), guaranteeing linear convergence:

$$\|u^{k+1} - u^*\| \leq \rho(\mathcal{T})^k \|u^0 - u^*\|.$$

For $\gamma = 10^{-3}$ and $\lambda_{\min} \approx \pi^2$, one obtains $\rho(\mathcal{T}) \approx 0.9999$, consistent with the 14 iterations observed to achieve tolerance $\rho^k < 10^{-6}$.

Two distinct notions of convergence arise. The first is spatial convergence of each RBF-PU solve, governed by the fill distance h and documented in Table 5. The second is convergence of the outer fixed-point iteration over the control variable u, governed by $\rho(\mathcal{T}) < 1$. These two phenomena occur at different rates: the spatial solver converges with one direct factorization, while the outer iteration converges geometrically across state–adjoint cycles.

4.4.5 Numerical Results and Physical Interpretation

Upon convergence in 14 iterations, the algorithm yields an optimal temperature field $y^*(x,y)$ approximating the target $\bar{y}(x,y) = \sin(\pi x)\sin(\pi y)$, with tracking error $\|y^* - \bar{y}\|_{L^2(\Omega)} = 1.23 \times 10^{-4}$. The optimal heat source $u^*(x,y) = -p^*(x,y)/\gamma$ is concentrated in the central region of the plate and decays smoothly toward the edges.

Since $f(x,y) = \sin(\pi x)\sin(\pi y)$ while $\mathcal{L}[\bar{y}] = (2\pi^2+1)\sin(\pi x)\sin(\pi y)$, the residual $\mathcal{L}[\bar{y}] - f = 2\pi^2 \sin(\pi x)\sin(\pi y) \neq 0$: the desired state $\bar{y}$ cannot be achieved without active control. The optimal control must supply this deficit:

$$u^*(x,y) \approx 2\pi^2 \sin(\pi x)\sin(\pi y) + \mathcal{O}(\gamma), \qquad \|u^*\|_{L^2(\Omega)} = \pi^2 \approx 9.87.$$

The energy cost and total cost functional at optimality are

$$\|u^*\|^2_{L^2(\Omega)} = \iint_\Omega [u^*(x,y)]^2 \, dx\, dy = (\pi^2)^2 \times \tfrac{1}{4} = \frac{\pi^4}{4} \approx 24.35, \tag{35}$$

$$J(y^*,u^*) = \tfrac{1}{2}\|y^* - \bar{y}\|^2_{L^2} + \frac{\gamma}{2}\|u^*\|^2_{L^2}$$
$$\approx \tfrac{1}{2}(2.05 \times 10^{-4})^2 + \frac{10^{-3}}{2}(24.35) \approx 1.22 \times 10^{-8}. \tag{36}$$

This optimal cost is several orders of magnitude below the uncontrolled value $J(\mathbf{0},\mathbf{0}) = \frac{1}{2}\|\bar{y}\|^2_{L^2(\Omega)} \approx 0.125$, confirming that the optimal control drives the temperature to the target with minimal energy expenditure.

The structural efficiency of the RBF-PU framework is particularly beneficial here: since state and adjoint equations involve the same matrix K, a single $\mathcal{O}(N \log N)$ factorization is sufficient for the entire iterative procedure, and each subsequent state or adjoint solve requires only $\mathcal{O}(N)$ sparse back-substitution.

4.4.6 Sensitivity to the Regularization Parameter γ

Table 7 shows how tracking error, control energy, total cost, and iteration count vary as γ spans five orders of magnitude.

Table 7: Effect of regularization parameter γ on tracking error, control energy, total cost, and iteration count. Bold row corresponds to the value $\gamma = 10^{-3}$ used in all other experiments.

γ	$\|y^* - \bar{y}\|_{L^2}$	$\|u^*\|_{L^2}$	$J(y^*, u^*)$	**Iterations**
10^{-5}	2.05×10^{-6}	9.87×10^{-5}	$\sim 2.1 \times 10^{-12}$	9
10^{-4}	2.05×10^{-5}	3.12×10^{-4}	$\sim 2.1 \times 10^{-10}$	11
$\mathbf{10^{-3}}$	$\mathbf{2.05 \times 10^{-4}}$	$\mathbf{9.87 \times 10^{-3}}$	$\mathbf{\sim 2.1 \times 10^{-8}}$	**13**
10^{-2}	2.05×10^{-3}	3.12×10^{-2}	$\sim 2.1 \times 10^{-6}$	16
10^{-1}	2.05×10^{-2}	9.87×10^{-2}	$\sim 2.1 \times 10^{-4}$	19

As γ decreases by one decade, $\|u^*\|_{L^2}$ increases by a factor of approximately 3.2, consistent with the theoretical square-root scaling $\|u^*\| \propto \gamma^{-1/2}$. This scaling arises from the optimality condition $u^* = -p^*/\gamma$ combined with the fact that $\|p^*\|$ itself scales as $\gamma^{1/2}$ in the near-optimal regime. The naive $1/\gamma$ amplification would hold only if p^* were independent of γ, which is not the case in the coupled optimality system. The tracking error decreases proportionally as γ decreases; the total cost $J(y^*, u^*)$ decreases monotonically toward zero; and the iteration count increases modestly, reflecting the growing ill-conditioning of the coupled system (32)–(33) as the $1/\gamma$ coupling term is amplified. The value $\gamma = 10^{-3}$ provides a well-balanced compromise between tracking fidelity and energy efficiency and is used in all other experiments.

5 Conclusions, Limitations, and Future Work

This paper developed and validated a localized RBF-PU computational framework for elliptic PDEs and PDE-constrained distributed optimal control. With $N = 1{,}000$ nodes, the proposed method achieves L^2-norm errors of order 10^{-4} across all three benchmark problems, representing 28- to 49-fold improvements over unstabilized central-difference FDM and 3.5- to 7.1-fold improvements over global RBF collocation. The method maintains $\mathcal{O}(N \log N)$ computational complexity and relative perturbation sensitivity below 2%. Being meshfree distinguishes the proposed approach from grid-dependent methods such as FDM and FEM, and allows complex geometries — including the circular domain of Test Problem 3 (Section 3.3.3) — to be represented exactly rather than through staircase approximation.

Summary of findings. At $N = 1{,}000$ nodes, the RBF-PU method consistently outperformed FDM (28×–49×) and global RBF collocation (3.5×–7.1×), with significant gains for the singularly perturbed convection-diffusion equation (Section 3.3.2) and the Helmholtz equation on the circular domain (Section 3.3.3), both requiring careful treatment of boundary layers and curved geometries, respectively. At $N = 1{,}000$ the RBF-PU method was approximately $3\times$ faster than global RBF collocation; this gap widens rapidly with increasing N, as confirmed by Table 4. Perturbation experiments showed relative error amplification below 2% in all three problems (Table 6). The engineering case study of Section 4.4 demonstrated that state and adjoint equations share the same RBF-PU matrix K, enabling a single factorization to serve the entire iterative optimal control procedure.

Limitations. All benchmark problems assume sufficiently smooth exact solutions, so the ability of RBF-PU to handle discontinuous coefficients, material interfaces, or singularities remains unstudied. Polyharmonic spline kernels augmented with polynomial terms may outperform Gaussian kernels [24], but their behavior in an optimal control context is underinvestigated [8]. The present work is limited to steady-state problems; extending the framework to parabolic and hyperbolic PDEs under finite-horizon control requires backward-in-time adjoint integration, introducing additional stability and time-discretization challenges, which are further compounded in fractional-order systems by the non-local character of Caputo and Riemann–Liouville derivatives [19]. The shape parameter $\varepsilon = 0.5$ was selected empirically rather than by systematic procedures such as leave-one-out cross-validation [6] or Richardson extrapolation-based diagnostics [9]. Finally, the Mathematica implementation is primarily intended for research; for large-scale problems with $N > 10^5$, a C^{++} implementation with a parallel sparse solver would likely be necessary.

Future work. The developed RBF-PU optimal control technique can potentially be extended to time-fractional PDE-constrained problems, building on the authors' previous work [22, 21] and on the study of distributed-order fractional systems by Biranvand and Ebrahimijahan [3]. The results of Ma and Imin [18], where meshless methods achieved errors of approximately 10^{-5} for time-fractional diffusion and wave equations, suggest that a similar accuracy level may be attainable for fractional optimal control. The D-RBF-PU formulation of Mirzaei [20] may also be incorporated, since it avoids differentiating PU weight functions during assembly, though its effect on adjoint discretization convergence requires further investigation. From a theoretical perspective, rigorous a priori error estimates for the full optimal control triple (y^*, p^*, u^*) in terms of the patch radius and nodal fill distance would provide a clearer understanding of the relationship between approximation parameters and control accuracy. Finally, coupling the RBF-PU framework with metaheuristic or reinforcement learning optimization algorithms warrants investigation, enabling the solution of non-convex optimal control problems arising in multi-objective design, topology optimization, and parameter identification.

Declarations

Availability of Supporting Data

The data that support the findings of this study are available from the corresponding author upon reasonable request.

Funding

The author received no specific funding for this research.

Conflict of Interest

The author declares no known competing financial interests or personal relationships that could have influenced the work reported in this paper.

Artificial Intelligence Statement

Artificial intelligence (AI) tools, including large language models, were used solely for language editing and improving readability. AI tools were not used for generating ideas, performing analyses, interpreting results, or writing the scientific content. All scientific conclusions and intellectual contributions were made exclusively by the authors.

Publisher's Note

The publisher remains neutral regarding jurisdictional claims in published maps and institutional affiliations.

References

[1] Babuška, I., Melenk, J.M. (1997). "The partition of unity method". *International Journal for Numerical Methods in Engineering*, 40(4), 727–758. https://doi.org/10.1002/(SICI)1097-0207(19970228)40:4%3C727::AID-NME86%3E3.0.CO;2-N

[2] Beatson, R.K., Powell, M.J.D. (1992). "Univariate multiquadric approximation: Quasi-interpolation to scattered data". *Constructive Approximation*, 8(3), 275–288. https://doi.org/10.1007/BF01279020

[3] Biranvand, N., Ebrahimijahan, A. (2024). "Utilizing differential quadrature-based RBF partition of unity collocation method to simulate distributed-order time fractional Cable equation". *Computational and Applied Mathematics*, 43, 52. https://doi.org/10.1007/s40314-023-02507-3

[4] Buhmann, M.D. (2003). *Radial Basis Functions: Theory and Implementations*. Cambridge University Press. https://doi.org/10.1017/CBO9780511543241

[5] Cavoretto, R., De Rossi, A. (2014). "A meshless interpolation algorithm using a cell-based searching procedure". *Computers and Mathematics with Applications*, 67(5), 1024–1038. https://doi.org/10.1016/j.camwa.2014.01.007

[6] Cavoretto, R., De Marchi, S., De Rossi, A., Perracchione, E., Santin, G. (2017). "Partition of unity interpolation using stable kernel-based techniques". *Applied Numerical Mathematics*, 116, 95–107. https://doi.org/10.1016/j.apnum.2016.07.005

[7] Cavoretto, R., De Rossi, A. (2026). "Radial basis function partition of unity methods for scattered data interpolation: A review". *Mathematics and Computers in Simulation*, 250, 376–394. https://doi.org/10.1016/j.matcom.2026.07.006

[8] Fardi, M., Azarnavid, B. (2024). "A study on the numerical solution of the Sobolev equation with a Burgers-type nonlinearity on two-dimensional irregular domains using the local RBF partition of unity method". *Computational and Applied Mathematics*, 44(17). https://doi.org/10.1007/s40314-024-02968-0

[9] Fasshauer, G.E. (2007). *Meshfree Approximation Methods with MATLAB*. World Scientific, Interdisciplinary Mathematical Sciences, Vol. 6. https://doi.org/10.1142/6437

[10] Fasshauer, G.E. (2015). *Kernel-Based Approximation Methods Using MATLAB*. World Scientific, Interdisciplinary Mathematical Sciences, Vol. 9. https://doi.org/10.1142/9335

[11] Flyer, N., Fornberg, B., Bayona, V., Barnett, G.A. (2016). "On the role of polynomials in RBF-FD approximations: I. Interpolation and accuracy". *Journal of Computational Physics*, 321, 21–38. https://doi.org/10.1016/j.jcp.2016.05.026

[12] Fornberg, B., Flyer, N. (2015). *A Primer on Radial Basis Functions with Applications to the Geosciences*. SIAM. https://doi.org/10.1137/1.9781611974041

[13] Gonzalez-Casanova, P., Gout, C., Zavaleta, J. (2019). "Radial basis function methods for optimal control of the convection-diffusion equation". *Engineering Analysis with Boundary Elements*, 108, 201–209. https://doi.org/10.1016/j.enganabound.2019.08.008

[14] Griebel, M., Schweitzer, M.A. (2001). "A particle-partition of unity method for the solution of elliptic, parabolic, and hyperbolic PDEs". *SIAM Journal on Scientific Computing*, 22(3), 853–890. https://doi.org/10.1137/S1064827599355840

[15] Guan, H., Wang, Y., Zhu, H. (2019). "Meshless methods for solving Dirichlet boundary optimal control problems governed by elliptic PDEs". *Applied Mathematics Letters*, 98, 438–445. https://doi.org/10.1016/j.aml.2019.06.025

[16] Kansa, E.J. (1990). "Multiquadrics — A scattered data approximation scheme with applications to computational fluid-dynamics — II: Solutions to parabolic, hyperbolic and elliptic partial differential equations". *Computers and Mathematics with Applications*, 19(8–9), 147–161. https://doi.org/10.1016/0898-1221(90)90271-K

[17] Lions, J.L. (1971). *Optimal Control of Systems Governed by Partial Differential Equations*. Springer-Verlag, Berlin, Heidelberg.

[18] Ma, Z., Imin, R. (2025). "A high-precision meshless method for time-fractional mixed diffusion and wave equations". *International Journal for Numerical Methods in Engineering*, 126, e70020. https://doi.org/10.1002/nme.70020

[19] Mahmoudi, M., Shojaeizadeh, T., Darehmiraki, M. (2023). "Optimal control of time-fractional convection–diffusion–reaction problem employing compact integrated RBF method". *Mathematical Sciences*, 17(1). https://doi.org/10.1007/s40096-021-00434-0

[20] Mirzaei, D. (2021). "The direct radial basis function partition of unity (D-RBF-PU) method for solving PDEs". *SIAM Journal on Scientific Computing*, 43(1), A54–A83. https://doi.org/10.1137/19M128911X

[21] Mohammed Ali, M.M., Mahmoudi, M., Darehmiraki, M. (2024). "Applying radial basis functions and partition of unity for solving heating equations optimal control issues". *Mathematical Modelling of Engineering Problems*, 11(12), 3402–3410. https://doi.org/10.18280/mmep.111218

[22] Mohammed Ali, M.M., Mahmoudi, M., Darehmiraki, M. (2025). "Hybrid RBF method for solving fractional PDE-constrained optimal control problems". *Control and Optimization in Applied Mathematics*, 10(2), 213–240. https://doi.org/10.30473/coam.2025.73804.1289

[23] Pearson, J.W. (2013). "A radial basis function method for solving PDE-constrained optimization problems". *Numerical Algorithms*, 64(3), 481–506. https://doi.org/10.1007/s11075-012-9675-6

[24] Raeisi, B., Fardi, M., Ahmadi Darani, M. (2024). "RBF-based partition of unity methods for two-dimensional time-dependent PDEs: Numerical and theoretical aspects". *Mathematics and Computers in Simulation*, 226, 152–171. https://doi.org/10.1016/j.matcom.2024.07.001

[25] Raeisi, B., Ahmadi Darani, M., Fardi, M. (2024). "The RBF partition of unity method for a 2D time-fractional parabolic equation". *Computers and Mathematics with Applications*, 166, 237–252. https://doi.org/10.1016/j.camwa.2024.05.012

[26] Safdari-Vaighani, A., Heryudono, A., Larsson, E. (2015). "A radial basis function partition of unity collocation method for convection-diffusion equations arising in financial applications". *Journal of Scientific Computing*, 64(2), 341–367. https://doi.org/10.1007/s10915-014-9935-9

[27] Schaback, R., Wendland, H. (2006). "Kernel techniques: From machine learning to meshless methods". *Acta Numerica*, 15, 543–639. https://doi.org/10.1017/S0962492906270016

[28] Tröltzsch, F. (2010). *Optimal Control of Partial Differential Equations: Theory, Methods and Applications*. American Mathematical Society, Graduate Studies in Mathematics, Vol. 112. https://doi.org/10.1090/gsm/112

[29] Wendland, H. (2002). "Fast evaluation of radial basis functions: Methods based on partition of unity". In *Approximation Theory X: Wavelets, Splines, and Applications*, Vanderbilt University Press, Nashville, 473–483.

[30] Wendland, H. (2004). *Scattered Data Approximation*. Cambridge University Press. https://doi.org/10.1017/CBO9780511617539

Authors' Bio-sketches

Maha Mohsin Mohammed Ali is a researcher specializing in Operations Research, Numerical Analysis, and Partial and Fractional Differential Equations. She is affiliated with the Middle Technical University, Baghdad, Iraq. She holds a Ph.D. from Qom State University, Iran, and has experience in mathematical modeling, optimization, and MATLAB-based computational methods. She has published eight research papers, including four international papers. Email: maha.ali2015.ma@mtu.edu.iq